Supporting Information

Iron complexes of an antiproliferative aroyl hydrazone: Characterization of three protonation states by EPR methods

*Andrei V. Astashkin, Rachel D. Utterback, Yu-Shien Sung, Elisa Tomat**

Department of Chemistry and Biochemistry, The University of Arizona, Tucson, AZ 85721

Contents **page**

Table S1. Crystallographic information for [Fe(AH1−*H*)(AH1−2*H*)]

Empirical formula	$C_{30}H_{25}FeN_4O_{2.5}S_2$
Formula weight/g mol^{-1}	601.51
Temperature/K	100.0
Crystal system	triclinic
Space group	P-1
a/Å	11.856(8)
b/Å	13.961(9)
c/Å	17.823(11)
α/°	93.86(2)
β/°	101.03(2)
γ/°	110.327(19)
Volume/Å^3	2686(3)
Z	4
ρ_{calc} g/cm^3	1.487
μ/mm^{-1}	0.756
F(000)	1244.0
Crystal size/mm^3	0.3 × 0.3 × 0.05
Radiation	MoKα (λ = 0.71073)
2Θ range for data collection/°	3.644 to 55.01
Index ranges	$-15 \leq h \leq 15$, $-18 \leq k \leq 17$, $-20 \leq l \leq 22$
Reflections collected	53096
Independent reflections	12154 [R_{int} = 0.0313, R_{sigma} = 0.0303]
Data/restraints/parameters	12154/18/739
Goodness-of-fit on F^2	1.000
Final R indexes [I>=2σ (I)]	R_1 = 0.0326, wR_2 = 0.1056
Final R indexes [all data]	R_1 = 0.0439, wR_2 = 0.1146
Largest diff. peak/hole / e Å^{-3}	0.50/-0.45

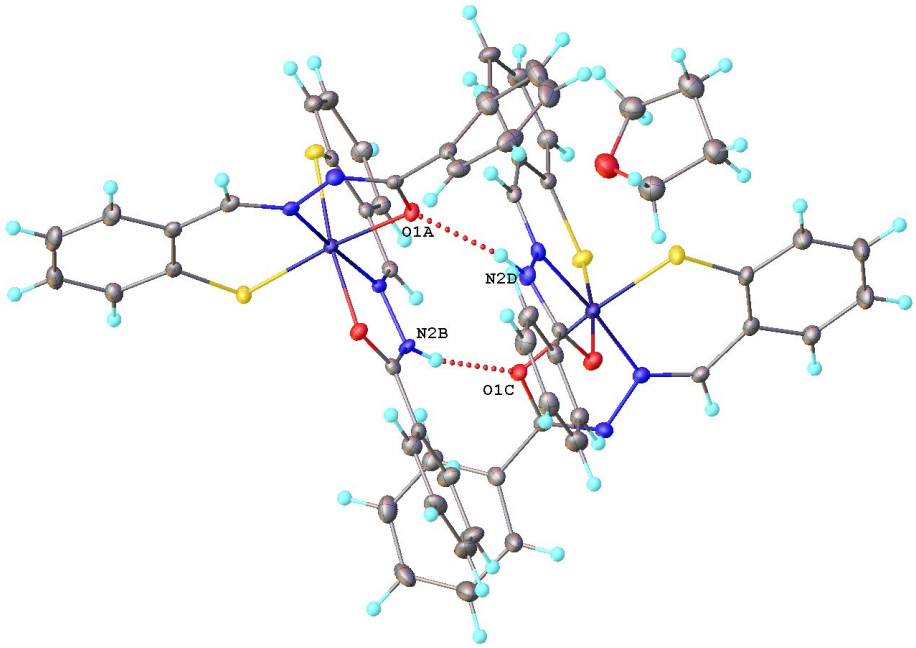

Figure S1. The unit cell of the Fe(III) AH1 crystal comprises two identical complexes. The ligands are labeled A and B on one complex, and C and D for the other complex. Ligands A and C are doubly deprotonated (AH1−2*H*). There are hydrogen bonds between O1A and the hydrogen at N2D and between O1C and the hydrogen at N2B. The co-crystallized THF molecule is disordered, and only one conformation is shown.

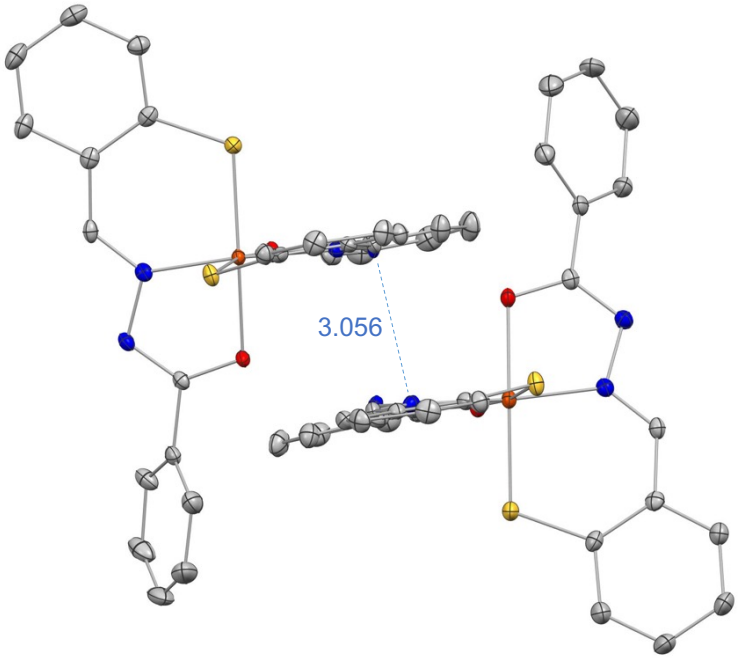

Figure S2. Stacking of the AH1 ligands in the crystal structure of [Fe(AH1−*H*)(AH1−2*H*)]. Thermal ellipsoids are at the 50% probability level. Carbon-bound hydrogen atoms in calculated positions are not shown.

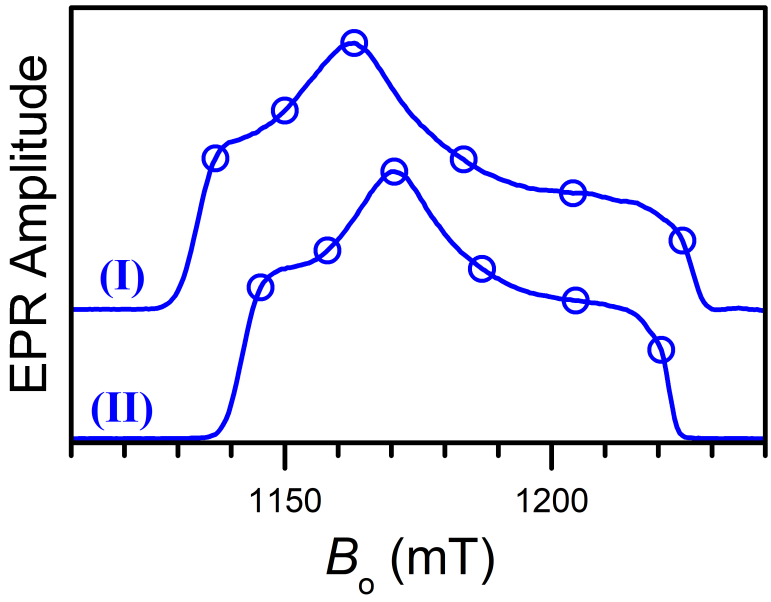

Figure S3. Two-pulse ESE field-sweep spectra of the iron AH1 complexes (species I and II). The spectra are the sums of those recorded at τ = 200 and 400 ns. Other experimental conditions: mw frequency, 34.268 GHz; mw pulse durations, 14 and 22 ns; temperature, 15 K. The circles indicate the positions of ESEEM measurements.

K_a-band pulsed EPR measurements on iron AH1 complexes I and II and calculation of the field-integrated ESEEM spectra

The two-pulse ESE field sweep spectra recorded at the microwave (mw) K_a-band are shown in Figure S3. The two-pulse ESEEM measurements were performed at the magnetic fields indicated by circles.

The orientation-selective two-pulse ESEEM spectra obtained by the cosine Fourier transformation (FT) of the time-domain ESEEM traces are shown in Figures S4 and S5. These spectra were used to obtain the field-integrated ESEEM spectra shown in Figure 4 of the manuscript. A field-integrated ESEEM spectrum approximates the spectrum that would be obtained for an orientationally non-selective measurement (i.e., either for the mw excitation bandwidth exceeding the EPR spectrum width or for a system with isotropic EPR spectrum). To calculate such a spectrum, the individual orientation-selective ESEEM spectra are multiplied by the factors equal to the relative amplitudes of the field-sweep spectrum at the measurement positions and added together.

The field-integration approach has been used in the literature to simplify the analysis of the electron-nuclear double resonance (ENDOR) spectra of ^{1}H and ^{2}H nuclei [1-4] and the spectra of dipole interactions between the electron spins [5]. A similar method can also be used in the present case of ESEEM from the weakly coupled ^{14}N. Here, however, one has to account for the fact that different parts of the ^{14}N ESEEM spectrum should be treated separately because the dominant lines in those regions depend on B_o differently. For example, the lines of $\Delta m_I = 1$ transitions dominating at the frequencies below 6 MHz (highlighted by the green background in

the spectra of Figures S4 and S5) depend on B_o in proportion to $\nu_N = g_N\beta_n B_o$ (where g_N is the nuclear g-factor of ^{14}N and β_n is the nuclear magneton): $\nu_{\alpha,\beta}^{\Delta m=1} \approx \nu_N \pm A/2$, where the nuclear quadrupole interaction is neglected.

The lines of $\Delta m_I = 2$ transitions depend on B_o in proportion to $2\nu_N$: $\nu_{\alpha,\beta}^{\Delta m=2} \approx 2\nu_N \pm A$. The high-frequency line of this type is located at the frequency of about 11.5 MHz (in the part of the spectra highlighted by the yellow background) and is directly observable. The low-frequency line is located at the frequency of about 3.5 MHz and is hidden under more intense lines of $\Delta m_I = 1$ transitions and combination lines. Finally, the well-resolved sum combination lines of the $\Delta m_I = 2$ transitions depend on B_o in proportion to $4\nu_N$. These lines are seen as the sharp features of negative amplitude located at the frequencies of about 15–16 MHz (in the part of the spectra highlighted by blue).

Thus, to calculate the field-integrated spectrum of, e.g., species I, corresponding to B_o = 1163 mT, the spectra obtained at B_o values differing from 1163 mT by ΔB_o are first preprocessed by translating the parts of the spectra shown against the green, yellow, and blue backgrounds by, respectively, $\Delta\nu_N = g_N\beta_n\Delta B_o$, $2\Delta\nu_N$, and $4\Delta\nu_N$, and only then multiplied by the appropriate scaling factors and summed up.

One has to note that the difference combination lines in the green region (negative peaks at 3–4 MHz), to first order, do not depend on ν_N, but are also shifted by $\Delta\nu_N$ in the preprocessing step. This, however, results in only a minor error because the largest $\Delta\nu_N$ value encountered in processing our K_a-band ESEEM data equals only 0.15 MHz (corresponds to the difference in magnetic fields between the middle (1171 mT) and high-field (1220.5 mT) EPR turning points for species II).

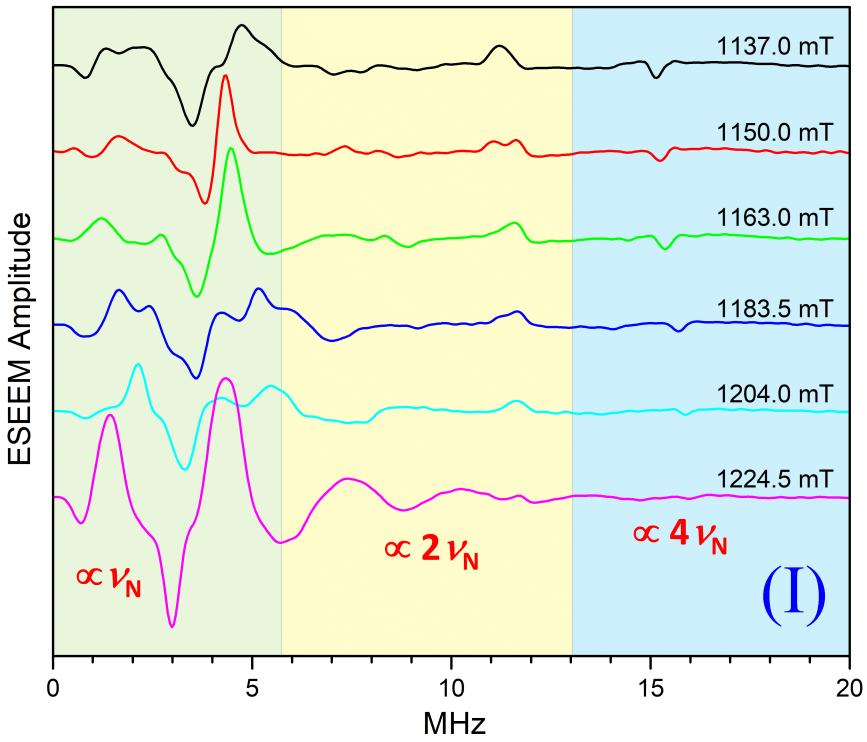

Figure S4. Two-pulse ESEEM spectra (cosine FT) of iron AH1 complex I obtained at several magnetic field positions across the field-sweep spectrum (as indicated by circles in Figure S3). Experimental conditions: mw frequency, 34.268 GHz; mw pulse durations, 14 and 22 ns; temperature, 15 K. For the calculation of the field-integrated spectrum corresponding to the effective B_o = 1163 mT (shown in Figure 4 of the main text), the parts of the spectra shown against the backgrounds of different colors were translated along the frequency axis in proportion with the changes in ν_N corresponding to the given change of B_o. The proportionality factors are indicated in the figure.

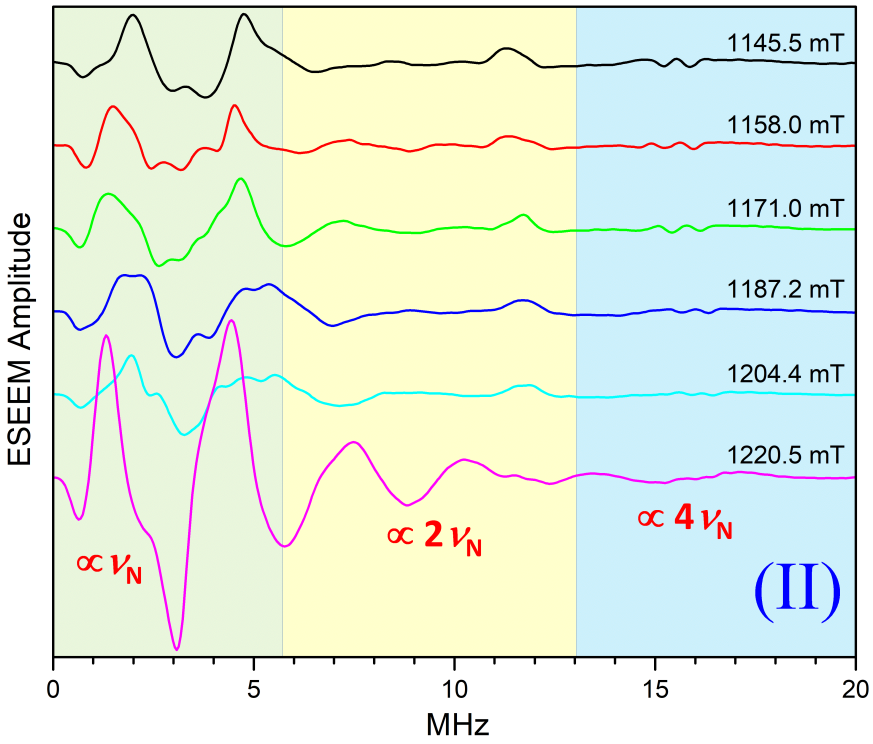

Figure S5. Two-pulse ESEEM spectra (cosine FT) of iron AH1 complex II, obtained at several magnetic field positions across the field-sweep spectrum (as indicated by circles in Fig. S3). Experimental conditions: mw frequency, 34.268 GHz; mw pulse durations, 14 and 22 ns; temperature, 15 K. For the calculation of the field-integrated spectrum corresponding to the effective B_o = 1171 mT (shown in Figure 4 of the main text), the parts of the spectra shown against the backgrounds of different colors were translated along the frequency axis in proportion with the changes in ν_N corresponding to the given change of B_o. The proportionality factors are indicated in the figure.

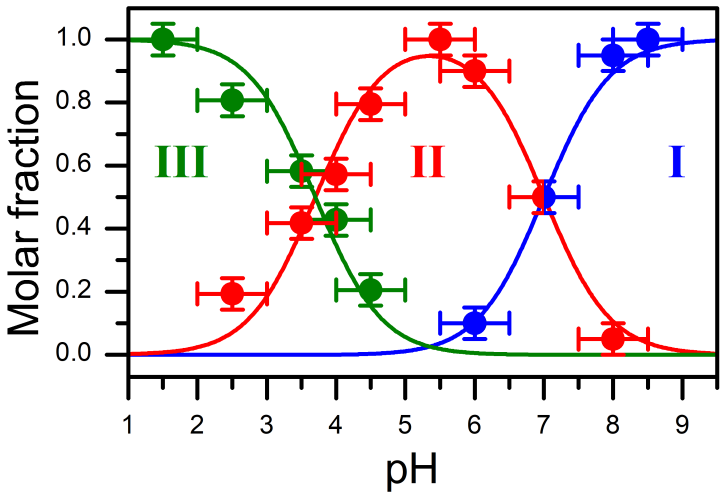

Figure S6. Relative amounts of Fe(III) AH1 complexes I, II, and III (200 μM) in 70/30% DMSO/water solutions at various pH values. The molar fractions were determined through deconvolution and integration of CW EPR spectra (see Figure 3 in the main text for examples). The pH values were estimated using colorimetric indicator strips with a sensitivity of 0.5 pH units. Only one or two complexes were reliably observed at each pH. Solid lines show the calculated molar fractions for protonation equilibria with $pKa_1 = 3.7$ and $pKa_2 = 7.0$.

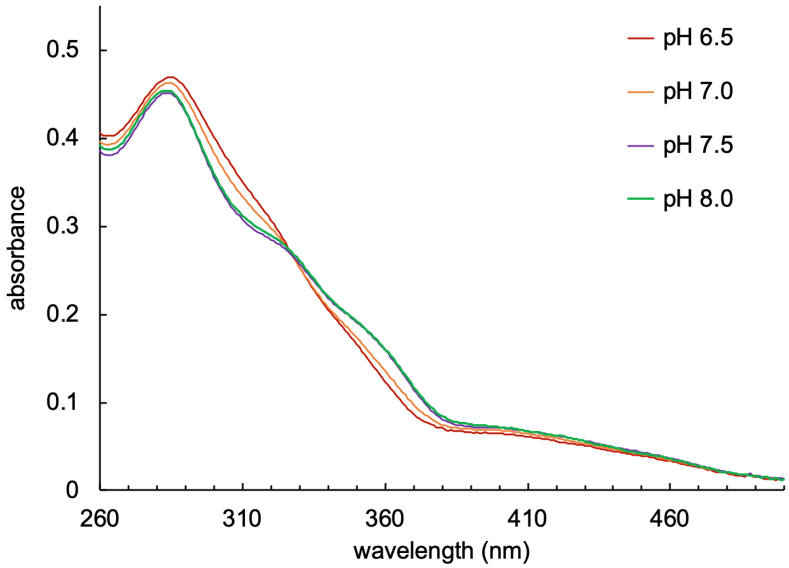

Figure S7. Optical absorption spectra of Fe(III) AH1 (15 μM) in 10% DMSO aqueous buffer solutions (50 mM PIPES for pH 6.5 and 7.0, 50 mM HEPES for pH 7.5 and 8.0).

References

1. Astashkin, A. V.; Klein, E. L.; Enemark, J. H., Toward Modeling the High Chloride, Low pH Form of Sulfite Oxidase: K_a-band ESEEM of Equatorial Chloro Ligands in Oxomolybdenum(V) Complexes. *J. Inorg. Biochem.* **2007**, *101*, 1623−1629.

2. Astashkin, A. V.; Johnson-Winters, K.; Klein, E. L.; Byrne, R. S.; Hille, R.; Raitsimring, A. M.; Enemark, J. H., Direct Demonstration of the Presence of Coordinated Sulfate in the Reaction Pathway of Arabidopsis Thaliana Sulfite Oxidase Using ^{33}S Labeling and ESEEM Spectroscopy. *J. Am. Chem. Soc.* **2007**, *129*, 14800−14810.

3. Astashkin, A. V.; Elmore, B. O.; Chen, L.; Fan, W.; Guy Guillemette, J.; Feng, C., Pulsed ENDOR Determination of the Arginine Location in the Ferrous−NO Form of Neuronal NOS, *J. Phys. Chem. A* **2012**, *116*, 6731−6739.

4. Astashkin, A. V.; Chen, L.; Elmore, B. O.; Kunwar, D.; Miao, Y.; Li, H.; Poulos, T. L.; Roman, L. J.; Feng, C., Probing the Hydrogen Bonding of the Ferrous−NO Heme Center of nNOS by Pulsed Electron Paramagnetic Resonance. *J. Phys. Chem. A* **2015**, *119*, 6641−6649.

5. Astashkin, A. V.; Rajapakshe, A.; Cornelison, M.; Johnson-Winters, K.; Enemark, J. H., Determination of the Distance between the Mo(V) and Fe(III) Heme Centers of Wild Type Human Sulfite Oxidase by Pulsed EPR Spectroscopy. *J. Phys. Chem. B* **2012**, *116*, 1942−1950.